Effect of Bimodal-Sized Hybrid TiC–CNT Reinforcement on the Mechanical Properties and Coefficient of Thermal Expansion of Aluminium Matrix Composites

Peter Nayno[1]r, Omayma El-Kady[2], Hossam M. Yehia[3], Atef S. Hamada[4], Mohsen A. Hassan[1]

Abstract

Aluminium (Al) matrix reinforced with carbon nanotubes (CNT), micron-sized titanium carbide (TiC) particles, and bimodal (nano + micron) hybrid TiC–CNT is fabricated by solution ball milling, followed by cold compaction and vacuum sintering to improve the mechanical properties and reduce thermal expansion. The hardness, wear resistance, compressive strength and CTE of pure Al, 0.6 wt% CNT/Al, 10 wt% TiC/Al, and hybrid 10–0.6 wt% TiC–CNT/Al composites have been investigated in this work. Analysis of strengthening mechanisms based on theoretical models, microstructure, and properties of constituent materials is performed. Microstructure analysis reveals an excellent distribution of the reinforcement phase and no new phase formation in sintered composites. The hardness value of bimodal TiC–CNT reinforced Al composite is significantly higher than monomodal TiC reinforced composite, reaching 2.3 times the hardness value of pure Al. Similarly, the wear resistance improved, and CTE reduced with CNT and TiC addition but is even significantly better in the hybrid reinforced composite. Experimental values of CTE show good agreement with the theoretical model. The strength and ductility of materials are mutually exclusive, but the compressive strength of pure Al has been doubled without significant loss in ductility through the use of bimodal-sized hybrid TiC–CNT reinforcement in this work.

Keywords Aluminium metal matrix composites · Powder metallurgy · Solution ball milling · Titanium carbide–carbon nanotubes · Bimodal-sized reinforcement · Mechanical properties

1 Introduction

Pure aluminium (Al) and its alloys serve as lightweight materials needed for automobile, aerospace and electronic applications but perform poorly due to its low mechani- cal strength and a high coefficient of thermal expansion (CTE) ($21 - 26 \times 10^{-6}$ K^{-1}) [1]. Generally, the properties of aluminium and its alloys can be improved by fabricating monomodal (nano or micron), bimodal (micron + nano), or hybrid ceramic particle reinforced aluminium matrix composites (AMCs). Hybrid AMCs have been well studied in the open literature [2–8]. The type of particulate reinforcement combination discussed in literature can be categorized into three: two synthetic ceramic materials, an industrial waste derivative with synthetic ceramic material, and an agro-waste derivative with synthetic ceramic material [2]. Aluminium matrix hybrid composites reinforced with CNT/SiCp [4], SiC/TiB_2 [5], Al_2O_3/B_4C [6], WC/GNs [7], rice husk ash/ Al_2O_3 [8], SiC/TiB_2 [9] have been studied for improving mechanical, tribological and corrosion properties.

Nano-sized particle reinforcements improve the mechanical properties of composites by dispersion strengthening with a considerable reduction in ductility. The effective volume fraction addition is kept around 1% due to difficulty in dispersion and reinforcement agglomeration in the matrix [10]. Micron-sized particles reinforcement volume fractions as high as 40% are achievable.

✉ Peter Nyanor
peter.nyanor@ejust.edu.eg

[1] Department of Materials Science and Engineering, Egypt-Japan University of Science and Technology, Alexandria 21934, Egypt

[2] Powder Technology Division, Central Metallurgical Research and Development Institute (CMRDI), Cairo 11421, Egypt

[3] Mechanical Department, Faculty of Industrial Education, Helwan University, Cairo 11795, Egypt

[4] Kerttu Saalasti Institute, University of Oulu, 85500 Nivala, Finland

However, the large size of the reinforcement causes a discontinuity in the matrix material, leading to the deterioration of the ductility of the composite [11]. Bimodal-sized reinforced composites take advantage of a high-volume fraction without a drastic reduction in ductility. The mixture of micron- and nano-sized (bimodal-sized) particles of the same reinforcement type is reported to have a significant influence on the mechanical properties of Al matrix composites [12, 13].

Recently, the enhancement of mechanical properties of AMCs with the simultaneous addition of bimodal-sized particles has been studied extensively [5]. Carvalho et al. [3, 4] demonstrated the increase in tensile and wear proper- ties of hybrid AlSi-2 wt%CNTs-5 wt%SiCp composite over only CNT or SiCp reinforced composites. The increase in wear resistance was attributed to the simultaneous effect of one strengthening mechanism contributed by the different length-scale (nano + micro) of the reinforcements or two different strengthening mechanisms from the reinforcements. However, the fracture strain was very low resembling a brittle fracture. Tan et al. [5] improved the yield and ultimate strength of Al matrix through addition of 10 wt% micro-sized SiC and wt% nano-sized TiB_2 particles by 23 and 64%, respectively. The fractured surface however showed signs of brittle fracture due to the large size (13 μm) of the SiC particles reinforcement. The properties of the micron-sized reinforced composites decline with increasing size of reinforcement particles, as reported by Chaubey et al. [14]. Synergistic enhancement of tensile strength to about 94% with dual-nano reinforcement of 0.5 vol%CNTs-0.5 vol%SiCp in Al matrix composite was achieved by Zhang et al. [15] through a successive application of ultrasonication (1 h), ball milling (4 h at 200 rpm), spark plasma sintering (630 °C for 1 h) and hot extrusion (400 °C). The reduction in fracture strain was, however, not as drastic as in the previous studies. However, dual-nano reinforcement of 0.7 vol%CNTs–3 vol%TiC in Al composite increased yield strength (108.2 to 264.3 MPa), but drastically decreased its ductility (elongation from 18.9 to 4.5) [16]. It can be concluded that the size and fabrication method are not the only contributors to composite ductility but a complex combination of multiple factors.

Carbon nanotubes (CNT) is well known for its excellent set of mechanical, electrical, thermal, biological, and catalytic properties [17], which makes it attractive to be used in reinforcing aluminium composites [18]. Titanium carbide (TiC) particles have not only good strength, wear resistance, stability at high temperature, but also good chemical inertness and thermal conductivity [19]. The addition of TiC to aluminium improves the measured density [19], which is an indication of a reduction in porosity. Bimodal-sized hybrid reinforcement of micro-sized TiC and CNT in Al matrix where the size of TiC is kept to one order lower than that of SiCp previously reported in the literature [3–5] may hold the key to maintaining ductility whiles increasing strength.

The good dispersion of reinforcements in the matrix phase remains a challenge, especially for nano-sized reinforcement like CNT [20]. Significant success has been achieved by solution ball milling [20], functionalization of CNT, modification of CNT surface with polymer [21], and surfactants [22]. Also, in-situ grown [23], graphene oxide assisted dispersion of CNT [24], high and low energy ball milling [25] has been explored. The ultimate goal is the uniform dispersion of reinforcement with a minimal detrimental effect on its structural integrity [26]. Solution ball milling combines the advantages of solution-based surface modification, mechanical ball milling, and flaky powder surface enlargement into one process [20]. The short ball milling time protects the reinforcement from excessive damage while milling under a solution minimize oxidation.

In this research, the individual and hybrid strengthen- ing effect of CNT (nano-sized) and TiC (micron-sized) reinforcements on the hardness, wear resistance, compressive strength, and CTE of powder metallurgy fabricated Al matrix composites are studied. The effects of the fabrication process on the morphology of prepared powder and sintered composites are observed and discussed.

2 Experimental Process

2.1 Materials and Methods

In this work, pure aluminium with 99.5% purity and an average size of 10 μm obtained from DOP Organik Kimya, Turkey is used as matrix material. CNT with an average diameter of 13 nm and 1–2 μm average length (nano-sized), and TiC with an average size of 2.5 μm (micron-sized) supplied by Japan New Metals Co. Ltd, are used as the reinforcement materials. Pure Al reinforced with only CNTs, or TiC was used as reference material. The fabrication process of bimodal-sized hybrid TiC–CNT/Al was carried out in two main steps. Figure 1 shows the schematic illustration of the composite powder preparation and consolidation process. In the first step, a mixture of 0.6 wt% CNT and 10 wt% TiC was dispersed in methanol by ultrasonication for 1 h. Al powder was added to TiC–CNT methanol solution to form a slurry. The obtained slurry was transferred into a 250 ml ZrO_2 jar and 100 g ZrO_2 milling balls of 10 mm diameter with a ball to powder weight ratio (BPR) of 10:1 added. Solution ball milling (SBM) was done for a total time of 2 h at 200 rpm in planetary ball milling machine (PM 400 Retsch GmbH, Germany). To prevent excessive heating and the possibility of cold welding of powder, rotation for 5 min followed by suspension for 5 min was repeated 23 times. The milled slurry is allowed to settle in a beaker, filtered, and then dried in an

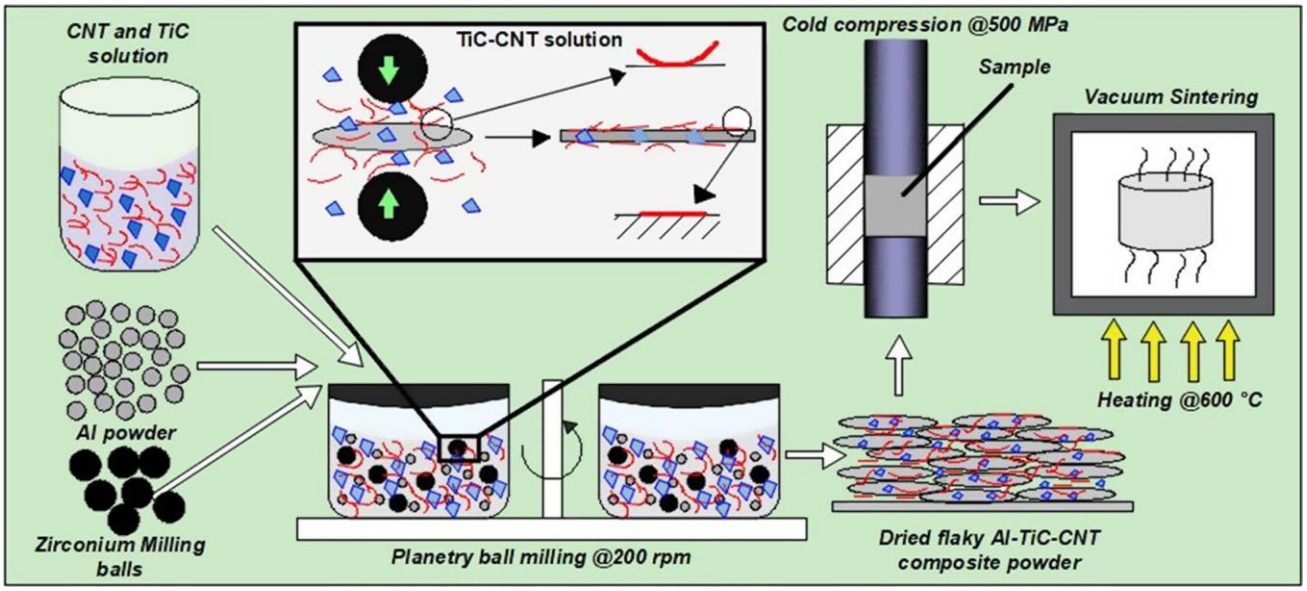

Fig. 1 A schematic illustration of the powder preparation and consolidation process

oven at 60 °C for 1 h. In the second step, the dried composite powder was compacted in a steel mould with 7.5 mm and 22 mm inner diameter under a pressure of 500 MPa using a uniaxial hydraulic compaction machine. Subsequently, the compacted composite materials are vacuum sintered at 600 °C. In the consolidation process, the specimens are heated in vacuum at the rate of 5 °C/min to 250 °C and held for 15 min to facilitate paraffin wax removal. After that, heating is continued at the same rate to 600 °C and soaked for 1 h at this temperature before cooling. Samples of pure Al, TiC (10 wt%)/Al, and CNT (0.6 wt%)/Al are also fabricated using the same conditions as reference materials. The fabricated composite materials were coded according to the content of CNT or TiC in wt%.

2.2 Characterization

The density of sintered composite specimens was measured using Archimedes' principle. Scanning electron microscope (SEM, JEOL JSM – 6010LV, Japan) equipped with energy-dispersive spectroscopy (EDS) and electron backscatter diffraction (EBSD) capabilities was employed to characterize the microstructure of the powder and fabricated composite materials. X-ray diffraction (XRD) was used to analyze the constituent phase structure of powder and sintered samples. A Shimadzu xlab 6100 diffractometer with Cu Kα radiation (V = 40 kV, I = 30 mA) at a scanning rate of 12°/min was used. Vickers hardness test measurements are performed on the Shimadzu hardness tester HMV-2, Japan by applying a force of 1.96 N for a loading time of 10 s. The reported values correspond to the mean of five measurements. The compressive strength of samples was measured by a universal testing machine (Shimadzu AG–X plus, Japan) at room temperature and strain rate of 0.001/s. Dry sliding wear test was performed on the TNO tribometer-block-on-ring wear test machine using ASTM G-77. The tested specimen dimensions prepared for wear test are 7 × 5 × 12 mm with its axis parallel to the pressing direction. The rotating sliding ring is made of 63 HRC steel with 73 mm diameter. A speed of 200 rpm and a force of 10 N is applied for 10 min. The wear rate is determined from the following equation:

$$\text{wear rate} = \frac{w_1 - w_2}{T} \quad (1)$$

where w_1 and w_2 are the weight of samples before and after wear tests respectively, T is test time.

The coefficient of thermal expansion of the deformed materials is measured by determining their thermal strain in the range of temperatures from 150 to 350 °C for 15 min on the test rig shown in Fig. 2 and evaluated using the following equation.

$$\alpha = \frac{L_2 - L_1}{(\Delta T) \times L_1} \quad (2)$$

where L_1 and L_2, are lengths of the composite sample before and after the heating, ΔT is the difference between the sample temperature and the room temperature.

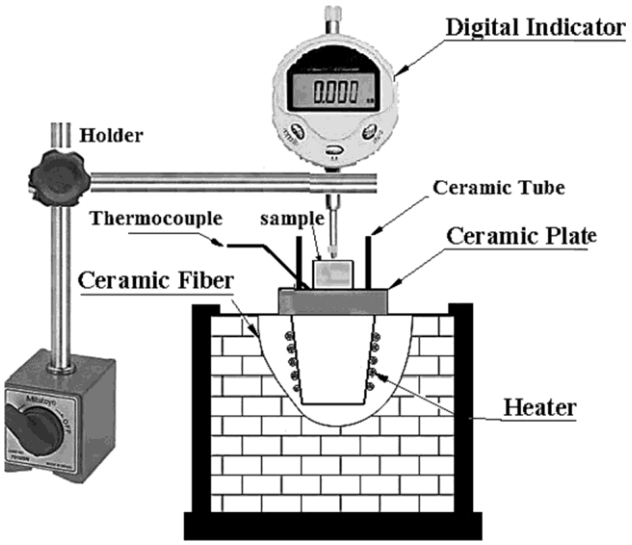

Fig. 2 Coefficient of thermal expansion test rig [27]

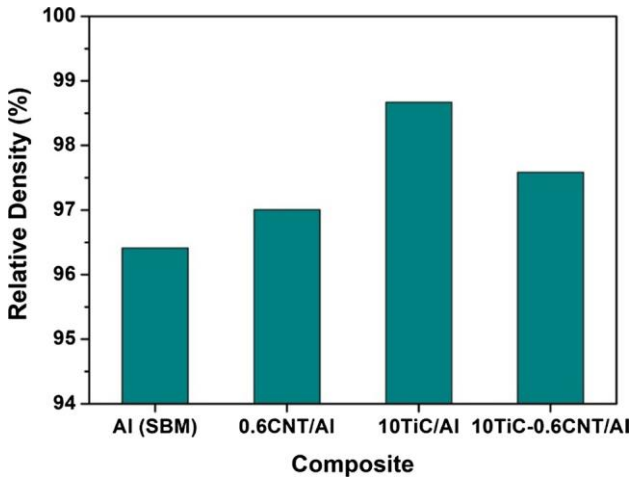

Fig. 3 Sintered composites' relative density variation with CNT, TiC and hybrid TiC–CNT reinforcement

3 Results and Discussions

3.1 Density of Sintered Samples

The density of sintered composites was measured by Archimedes' principle. The theoretical density of samples was calculated by the rule of mixtures, taking the density of Al, CNT, and TiC as 2.7 g/cm^3, 2.2 g/cm^3 [28], and 4.9 g/cm^3 respectively. The relative densities of the various composites are plotted in Fig. 3. Pure Al has the lowest relative density of 96.4% due to the significant morphological transformation of spherical Al particles to flakes during milling. The flakes reduce powder packing and provide considerable inter-particle friction during compaction. The density of CNT/Al composite increased over pure Al owing to nano-sized reinforcements' ability to effectively fill up microvoids at lower volume fractions increasing densification but turn to agglomerate at high volume fractions decreasing density [29]. TiC/Al composites reached the highest relative density of 98.6%. The high density of TiC particles, in comparison with that of Al, improves the overall composite density [30]. The hybrid TiC–CNT/ Al composite's relative density lies between that of CNT/ Al and TiC/Al. The presence of CNTs dispersed in the Al matrix gives high densification due to the interstitial distribution of it in the internal voids. Still, the presence of ceramic material like TiC acts as an interior barrier that restricts the complete densification. So, the density of the hybrid sample is more than that of Al, but less that of 10TiC/Al sample.

3.2 Microstructure of Composites

Figure 4 shows the microstructure of the as-received CNT, Al, TiC, and the solution ball-milled Al powder, respectively. The TEM image of CNT is shown in Fig. 4a and SEM images of pure Al particles (Fig. 4b), titanium carbide particles (Fig. 4c), and flake Al particles (Fig. 4d) produced by the SBM process are presented. There are some almost spherical Al particles due to the relatively short ball milling time used. The short ball milling time is to ensure the structural integrity of the CNT and TiC reinforcement is maintained after milling [26]. Long milling time leads to Al particles strain hardening and fracture, producing a large number of small particles [31]. The CNT and TiC reinforcement particles can also be damaged or even fractured under the impact of milling balls [32], thereby affecting their structural integrity. Figure 5 shows the morphology of the as-SBM pure Al and composite powders. Some level of CNT dispersion was achieved by this method as individual CNTs (red arrows) can be seen on the laky Al surface in Fig. 5b for 0.6CNT/Al composite powder. The micron-TiC particles (yellow arrows) were well distributed and embedded on the Al surface both in the 10TC/Al and 10TC-0.6CNT/Al hybrid reinforced composite powder of Fig. 5c, d. Also, some single and bundled strands of CNTs are observed on the Al surface in addition to TiC particles in the hybrid composite powder.

The SEM images of sintered Al and CNT, TiC, and hybrid TiC–CNT reinforced composites are shown in Fig. 6. CNTs are embedded in Al during milling and can hardly be seen in the SEM image. The images generally show uniform distribution of TiC particles in the Al matrix. Few TiC clusters can be seen as indicated by yellow dash circles in Fig. 6c, d. Careful observation of the hybrid composite at high magnification reveals pockets of CNT agglomeration (Fig. 6e). The EDS image of Fig. 6f shows an overlay of the

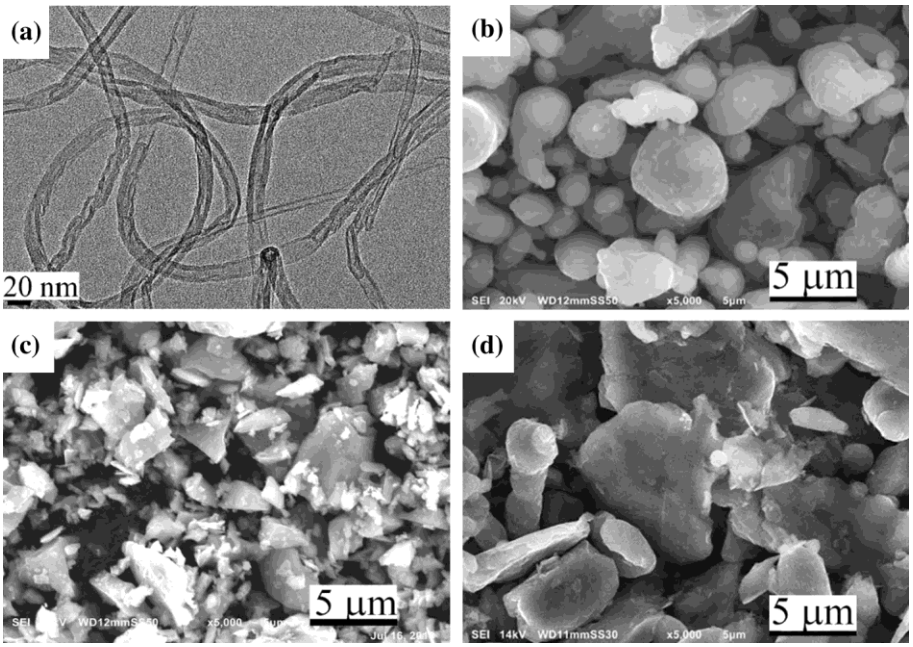

Fig. 4 **a** TEM image of raw CNT; SEM morphologies of raw materials, **b** pure Al powder, **c** TiC, **d** solution ball-milled pure Al powder

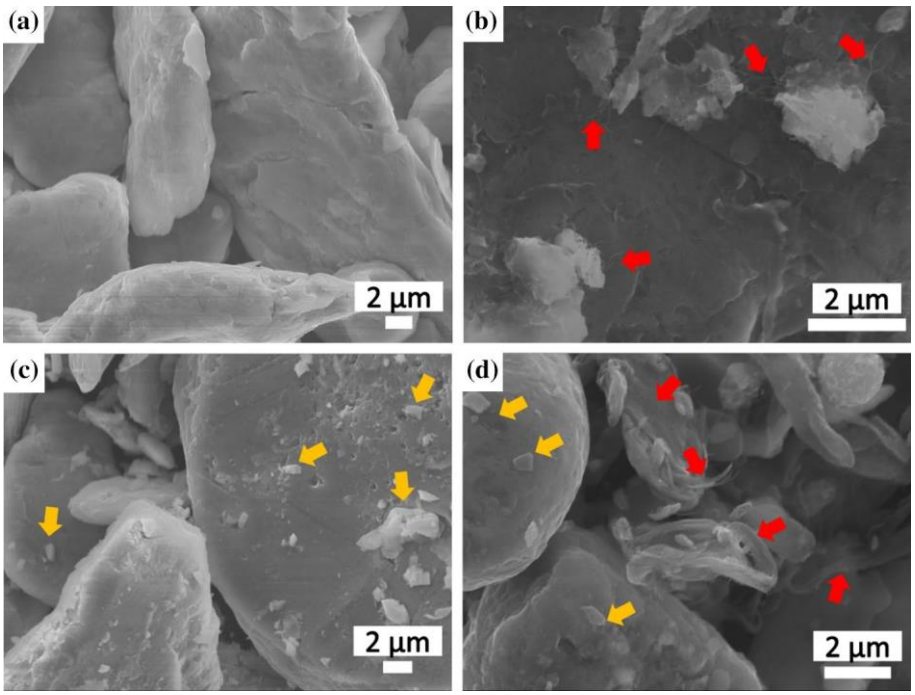

Fig. 5 SEM morphologies of SBM composite powder **a** flaky Al powder, **b** Al + 0.6 wt% CNT , **c** Al + 10 wt% TiC , **d** Al + 10 wt% TiC + 0.6 wt% CNT

various constituent of the composite, that is, Al, TiC, and CNT.

The grains of the sintered Al and composites are not equi-axed. The EBSD maps shown in Fig. 7 reveal the grain size varies from about 5 to 15 µm. The CNT/Al composite has the smallest average grain size of about 5 µm.

Figure 8 presents XRD patterns of raw powder samples and sintered composites from CNT/Al, TiC/Al, and hybrid TiC–CNT/Al samples. The weak carbon peak appears at about 25° in CNT powder. The TiC powder has peaks at 2θ of 35.91°, 41.71°, 60.45°, 72.34° and 76.11° corresponding to [111], [200], [220], [311] and [222] planes of face-centred cubic (FCC) TiC (illustrated in black circles). Strong peaks appeared at 2θ of 38.3° (111), 44.5° (200), 64.9° (220) and 78.0° (311) corresponding to face-centred cubic (FCC) Al. The presence of the second phase at the interface is reported by some researchers to negatively affect the strength of the composite [33, 34]. In contrast, others reported that it

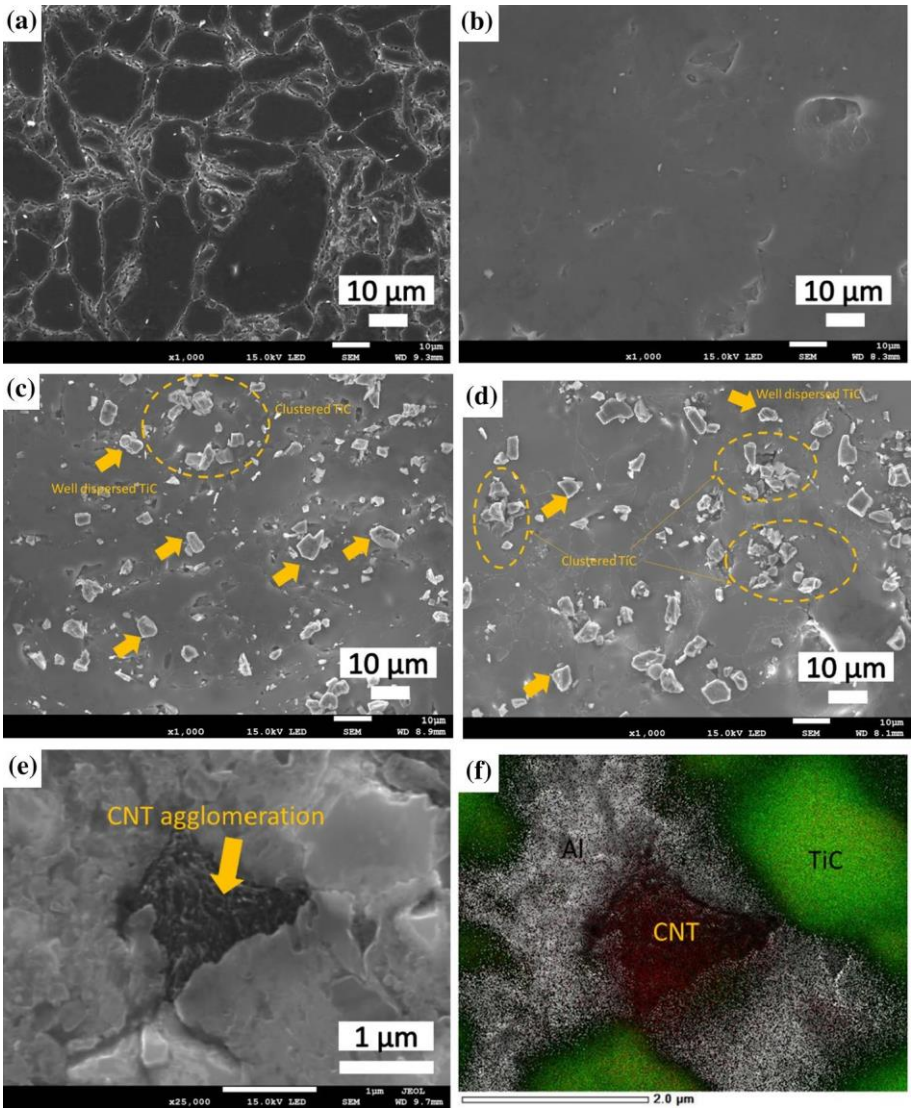

Fig. 6 SEM images of sintered composites of **a** Al, **b** 0.6CNT/Al, **c** 10TiC/Al, **d** hybrid 10TiC–0.6CNT/Al, **e** CNT agglomeration in hybrid 10TiC–0.6CNT/Al at high magnification, **f** EDS analysis of **e** showing the three compositions

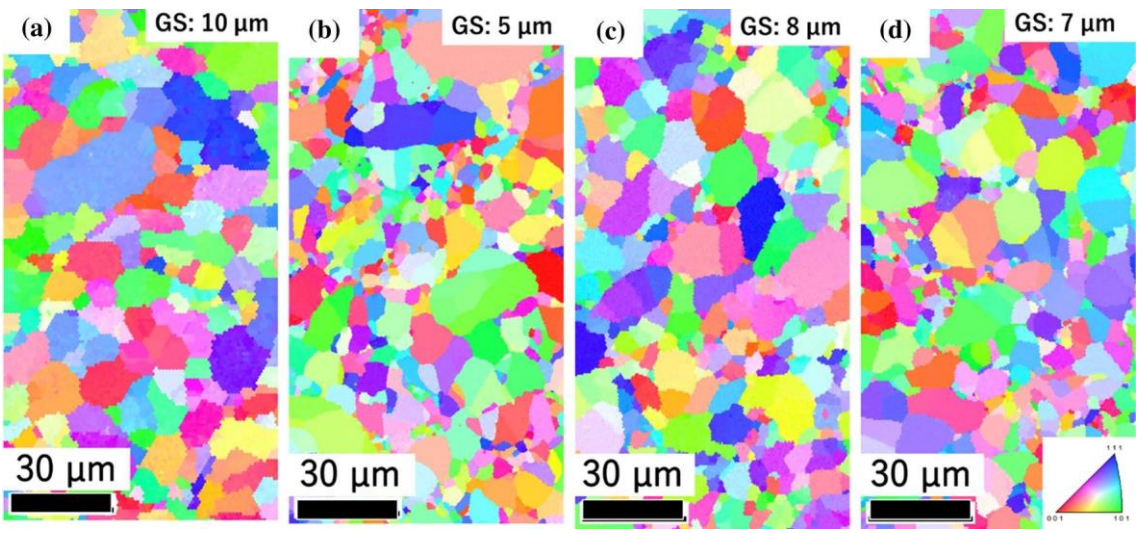

Fig. 7 EBSD map of **a** Al, **b** 0.6CNT/Al, **c** 10TiC/Al, **d** 10TiC–0.6CNT/Al composites

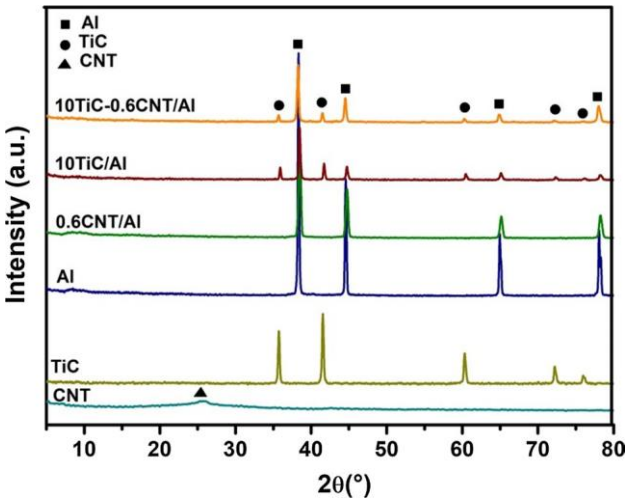

Fig. 8 XRD pattern of raw powder samples and sintered CNT, TIC and hybrid TiC–CNT reinforced aluminium matrix composites

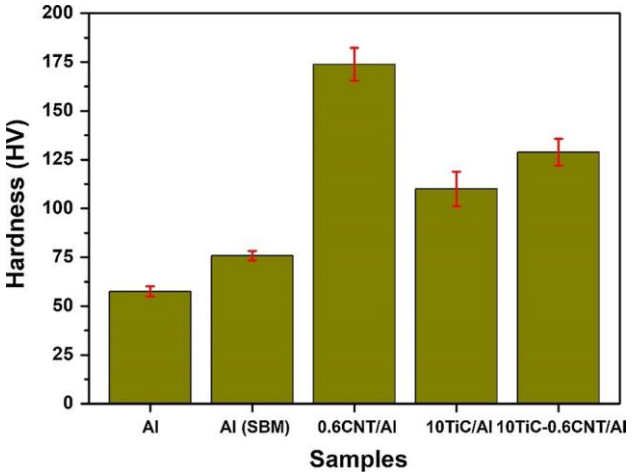

Fig. 9 The mean Vickers hardness of Pure Al samples, CNT/Al, TiC/Al, and hybrid TiC–CNT/Al composites

improves the interfacial bond strength, thus increasing load transfer [35, 36]. In the present work, aluminium oxide and carbide phases are not detected by XRD analysis. At sintering temperature above 600 °C, a high-resolution transmission electron microscope (HRTEM) detected Al_4C_3 in spark plasma, and vacuum sintered CNT/Al specimens [21, 37]. The interfacial reaction between the Al matrix and carbon atoms released by defective regions of TiC or CNT results in Al_4C_3 formation [1, 21, 37]. Liu et al. [37], used XRD and HRTEM to show that Al_4C_3 is observed in CNT/Al composites fabricated from powder mixture ball-milled over 4 h and not detected for shorter milling times. Therefore, it is proposed that the milling and vacuum sintering experimental conditions adopted in this work were mild enough to avoid Al_4C_3 formation.

3.3 Mechanical properties

3.3.1 Influence of CNT, TiC and Hybrid TiC/CNT Reinforcement on the Hardness

The hardness of Al composites reinforced with CNT, TiC, and hybrid TiC–CNT are measured using a Vickers hardness tester. The composites show increased resistance to localized deformation of the matrix during indentation as a result of the presence of the reinforcement phase [38]. In Fig. 9, sintered as-received pure Al has a hardness of 57.4 ± 2.6 HV while that of SBM pure Al has 75.8 ± 2.4 HV. The formation of flake shape Al particles from milling increased the hardness of Al by about 32%. The reduction in Al particle size during milling introduces grain refinement strengthening of the matrix according to the Hall–Petch effect. The hardness values (percentage increase over SBM pure Al) of 0.6CNT/Al, 10TiC/Al and 10TiC–0.6CNT/Al composites were 173.8 ± 8.3 HV (129.1%), 110 ± 8.8 HV (44.9%) and 128.8 ± 6.8 HV (69.8%), respectively. The 0.6CNT/ Al composite records the highest hardness, but its hardness value decreased on adding micron-TiC particles owing to the change in grain size. Grain size turns to be smaller in nano-reinforced composite compared to micro-reinforced composites, as clearly revealed by Fig. 7. The presence of ceramic particles with high strength uniformly distributed in the Al matrix leads to increase hardness according to the rule of mixture. The CNTs and TiC particles act as obstacles at grain boundaries to effectively hinder dislocation movement producing dislocation strengthening [31]. Also, the large surface area obtained from flaky Al particles improves the dispersion of both CNTs and TiC reinforcements in the Al matrix, leading to increased hardness value due to their high intrinsic hardness.

3.3.2 Influence of CNT, TiC and Hybrid TiC–CNT Reinforcement on Wear Resistance

The wear rate of CNT/Al, TiC/Al, and hybrid TiC–CNT/ Al composites are measured and presented in Fig. 10. Generally, the wear resistance was improved in all composites over the pure Al sample. Wear rate (percentage reduction) for pure Al, 0.6CNT/Al, 10TiC/Al and 10TiC–0.6CNT/Al composites are 0.239 mg/s, 0.012 mg/s (94.9%), 0.030 mg/s (87.4%), and 0.0083 mg/s (96.5%), respectively. CNTs improve hardness (Fig. 9) and also possess self-lubrication property [39], which acts to reduce friction between composite sample and the adhesive wheel, consequently improving the wear resistance of CNT/Al composite. Poor interfacial bonding between TiC and Al matrix slightly hinders wear resistance of TiC/Al composites as some TiC particles

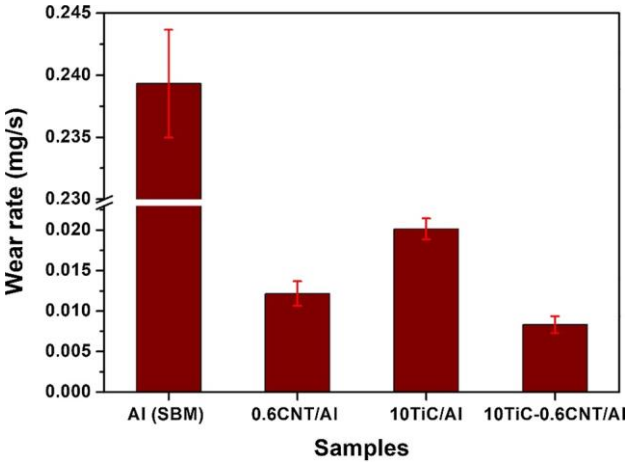

Fig. 10 Wear resistance of Al composites reinforced with CNT, TiC and hybrid TiC–CNTTiC–CNT

are easily removed; consequently, wear rate is increased. The non-wettability between TiC (a ceramic) and Al (a ductile metal) prevents good adhesion and contact at interface. The improved hardness of the hybrid TiC–CNT composite works to decrease the friction coefficient, thus improving wear resistance. Also, a good distribution of CNT in the Al matrix filling the pores enhances the wear resistance.

3.3.3 Influence of CNT, TiC and Hybrid TiC–CNT Reinforcement on Compressive Strength

Room temperature compression test for all samples revealed a significant improvement in the compressive yield strength (0.2% CYS) and ultimate compressive strength (UCS) by the addition of CNT, TiC, and hybrid TiC–CNT reinforcement to Al matrix. The results are summarized in Fig. 11 and

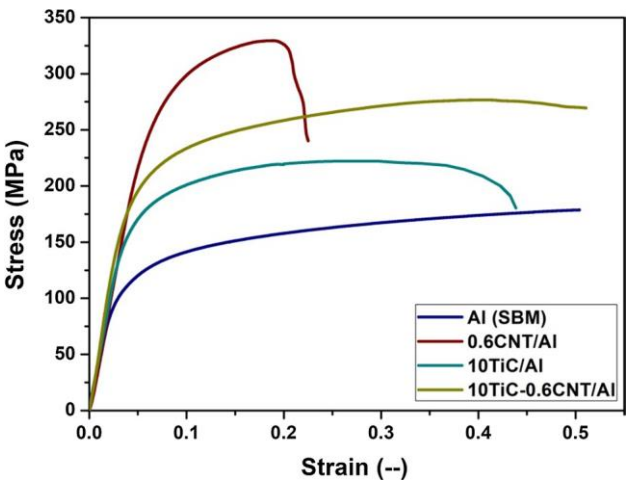

Fig. 11 Compression stress–strain curves for pure Al, CNT/Al, TiC/Al and hybrid TiC–CNT/Al composites

Table 1. The 0.6 CNT/Al composite recorded the highest 0.2% CYS of 202.74 MPa and UCS of 303.6 MPa. However, the strain to fracture decreased significantly to 21.2%, while pure Al samples did not fracture after 50% compression. The addition of CNTs leads to work-hardening and significantly reduces fracture strain (elongation). The vast difference between the intrinsic strength of the Al matrix and CNT may induce mismatch dislocations at the interface during compression. These dislocations can prevent movement of other generated dislocations, resulting in increased work-hardening [40]. Micron-sized TiC improved composite strength with CYS (percentage increase over pure Al) 150.5 MPa (82%) and UCS of 218.9 MPa. The fracture strain, on the other hand, was as high as 36.5%. Micron-sized reinforcement strengthening does not involve significant load transfer and grain refinement [15]; therefore the mismatch between CTE of Al matrix and TiC reinforcement particles promotes dispersion strengthening mechanism in the composite, thus hindering dislocation movement in the pure Al matrix to increase strength [41]. However, ductility decreases with increasing reinforcement particles size; the relatively small size of the TiC particles (average of 2.5 μm) used in comparison to Tjong et al. [11] may be the reason for retained ductility. In Fig. 11, hybrid 10TiC–0.6CNT reinforced Al matrix composite shows the same compressive stress–strain trend as 10TiC because TiC controls the plasticity of the composite. The CYS, UCS, and strain to fracture of the hybrid composite are 175.7 MPa, 277.16 MPa, and 41.8%, respectively. This represents 107.7% improvement in CYS in comparison to pure Al. The CYS, however, increased by only 16.7% when compared with 10TiC/Al composite. A more effective CNT dispersion method, such as physio-chemical dispersion, may be needed to ensure uniform distribution of CNT. The increased amount of CNTs taking part in dislocation strengthening and load transfer may result in synergistic improvement of strength. There is a synergistic improvement of compressive strength as observed in dual nano-sized reinforcements [15, 16, 42], but a trade-off between strength and ductility for bimodal-sized reinforced composites are obtained. Improved strength owing to CNTs and improved plasticity owing to micron-sized TiC are obtained

Table 1 Summary of mechanical properties of CNT/Al, TiC/Al and hybrid TiC–CNT/Al composites at room temperature

Sample	0.2% CYS	UCS	Fracture strain	Vickers Hardness
	MPa	MPa	%	HV
Pure Al	84.6	–	–	75.8 ± 2.4
0.6CNT/Al	202.74	303.60	21.2	173.8 ± 8.3
10TiC/Al	150.51	223.22	34.0	110 ± 8.8
10TiC–0.6CNT/Al	175.75	277.16	41.8	128.8 ± 6.8

for bimodal-sized hybrid TiC–CNT reinforcement. High fracture strain is beneficial to enhance crack propagation resistance in composite structure [43]. Figure 12a reveals the pure Al did not show any signs of surface cracks after 50% strain. The CNT/Al, TiC/Al, and hybrid TiC–CNT/ Al composites, however, show surface crack propagating along a 45° angle to the compression axis, as depicted in Fig. 12b–d. The SEM of the fractured surface of the TiC/Al composite indicates the presence of more shear bands. This can indicate the absence of debonding between matrix and

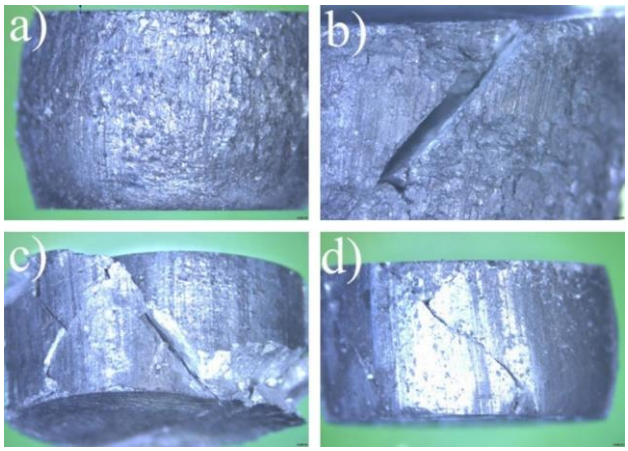

Fig. 12 Measuring microscope images of representative compression samples after testing **a** pure Al, **b** 10TiC/Al, **c** 0.6CNT/Al, **d** hybrid 10TiC–0.6CNT/Al composites

reinforcement (Fig. 13a–c). The hybrid composite fractured surface is shown in Fig. 13d–f have dimples, tear ridges, interfacial cracks, and some shear bands. This suggests a mixed-mode of shear and brittle failure consistent with the results of Habibi et al. [44] and Akinwekomi et al. [45].

3.3.4 Strengthening mechanisms of CNT/Al and TiC/Al composites

Grain refinement, thermal expansion coefficient (CTE) mismatch generated dislocation strengthening, load transfer, and the Orowan looping system are the four main strengthening mechanisms expected in ceramic reinforced metal matrix composites [35]. The overall strengthening contribution from the reinforcement is attributed to the simultaneous occurrence of these mechanisms, expressed in the formula [35]:

$$\Delta\sigma_c = \Delta\sigma_{GR} + \Delta\sigma_{CTE} + \Delta\sigma_{LT} + \Delta\sigma_{Orowan} \quad (3)$$

where $\Delta\sigma_c$ is the strength improvement of the composite, $\Delta\sigma_{GR}$ is a contribution to strength from grain refinement, $\Delta\sigma_{CTE}$ is the increase in strength provided by generation of dislocations due to CTE mismatch between matrix and reinforcement, $\Delta\sigma_{LT}$ is enhanced strength from load transfer from matrix to reinforcement and $\Delta\sigma_{Orowan}$ is strength improvement from Orowan looping system.

The overall yield strength of the composite can be estimated from the equation [46]:

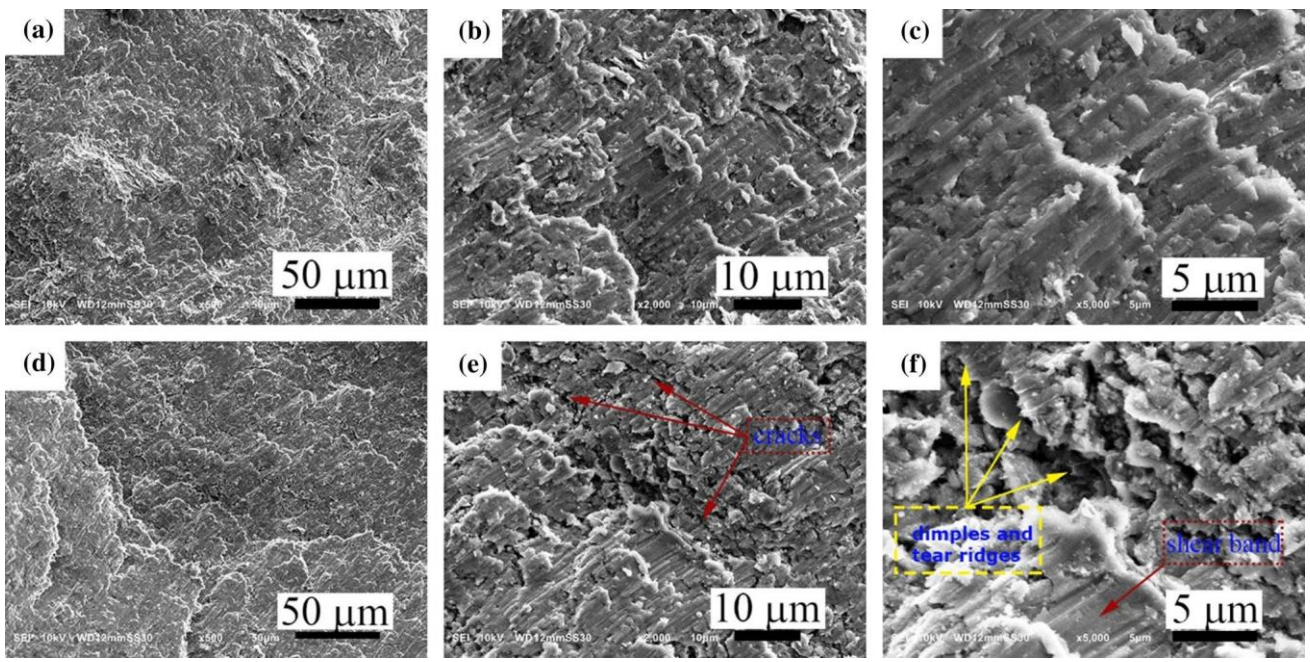

Fig. 13 SEM of the fractured surface after compression at different magnifications **a**–**c** 10TiC/Al composite, **d**–**f** hybrid 10TiC–0.6CNT/Al com-

posite

$$\sigma_y = \sigma_m + \Delta\sigma_c \tag{4}$$

where σ_y is the compressive yield strength of composite and σ_m is the compressive strength of the matrix.

To further understand the contribution of each of the strengthening mechanisms to the yield strength of CNT/Al and TiC/Al composites, theoretical calculations based on the composite microstructure are performed.

Reduction in grain size from ball milling and grain refinement during sintering owing to the pinning effect of the reinforcement phase against movement of grain boundaries can lead to composite strengthening known as the Hall–Petch effect [47].

$$\Delta\sigma_{GR} = k\left(d_c^{-1/2} - d_m^{-1/2}\right) \tag{5}$$

where d_c and d_m are the composite and matrix grain size respectively, and k is a constant (0.07 MPa $m^{1/2}$ for pure Al [16]). Using the average grain sizes presented in Fig. 7, the value of $\Delta\sigma_{GR}$ is estimated.

During sintering, dislocations are produced due to the significant mismatch between the CTE of the reinforcement phase and the matrix phase. The movement of the increased dislocation density within the matrix leads to composite strengthening. This effect can be expressed using the following equation [48]:

$$\Delta\sigma_{CTE} = 1.25Gb\sqrt{\frac{12V_f\Delta CTE\Delta T}{bd_p}} \tag{6}$$

where G is the shear modulus of the matrix (26.9 GPa [16]), b is the Burgers vector for matrix (0.286 [16]), V_f is volume fraction of reinforcement, ΔCTE is difference between room temperature CTE of matrix (23.6×10^{-6} K^{-1}) and reinforcement phases (0.9×10^{-6} K^{-1} for CNTs and 8.7×10^{-6} K^{-1} for TiC) [16, 30, 36, 38], ΔT is the difference between sintering and testing temperature (575 °C) and d_p is the effective reinforcement particle diameter. For CNT/Al composite, d_p can be obtained by assuming a spherical model for CNTs from $d_{p(CNTs)} = \sqrt[3]{\frac{3Sl_{CNT}}{4\pi}}$, where S and l_{CNT} are cross sectional area and length of CNT respectively [49]. The estimated $d_{p(CNTs)}$ is 56 nm and $d_{p(TiC)}$ is taken as 1.2 μm.

from the experiment) respectively. In the case of CNT, the following formula proposed by Kelly and Tyson [51] was employed:

$$\Delta\sigma_{LT} = \sigma_f V_f\left(\frac{l}{2l_c}\right) - \sigma_m V_f \quad \text{for } l \le l_c \tag{8}$$

$$\Delta\sigma_{LT} = \sigma_f V_f\left(1 - \frac{l}{2l_c}\right) - \sigma_m V_f \quad \text{for } l > l_c \tag{9}$$

where l_c, the critical length is given by:

$$l_c = \frac{\sigma_f d_p}{2r_m} \tag{10}$$

where σ_f is the yield strength of CNT (3.6 GPa [52]), and r_M is the ultimate shear strength of matrix material calculated from the ultimate yield strength. The improvement in yield strength of composite due to inhibition of dislocations propagation by reinforcement phase can be explained by the Orowan looping system. This increase can be calculated by the Orowan–Ashby equation [53]:

$$\Delta\sigma_{Orowan} = \frac{0.13Gb}{\lambda}\ln\left(\frac{d_p}{2b}\right) \tag{11}$$

where λ is the effective planar inter-particle spacing estimated by $\lambda = \left(\frac{1}{2V_f}\right)^{\frac{1}{3}} - 1\, d_p$. The overall strength of the composites estimated by Eq. (3) is $\sigma_{y(CNT\text{-}Al)} = 206.99MPa$ and $\sigma_{y(TiC\text{-}Al)} = 158.44MPa$, which is approximately 3.5% and 3.2% more than experimental results for these compos- ites. The estimated strength of the hybrid composite was evaluated using the quadrature method as supposed to direct addition [54]. In hybrid composite, the individual reinforcement acts to improve the properties as well as complement each other. For example, the grains are more refined in hybrid composites compared to TiC reinforced composites (Fig. 7). Since the actual interaction between the two reinforcement phases is not well understood, the overall strength of the hybrid composite is expressed by Eq. (9) as:

$$\sigma_{y(TiC-CNT\text{-}Al)} = \sigma_m + \sigma_{GR} + \Delta\sigma_{LT} + \sqrt{\Delta\sigma_{CTE}^{\,2} + \Delta\sigma_{Orowan}^{\,2}}$$

The modified shear-lag model is frequently used in estimating the load transferred from the matrix to the reinforcement phase. The interfacial bond strength between matrix and reinforcement affects how much load can be transferred. The load transfer contribution to increase in yield strength for particulate reinforcement can be expressed as [50]:

$$\Delta\sigma_{LT} = pV_f\sigma_m \tag{7}$$

where p and σ_m are aspect ratio of reinforcement (CNT = 50 and TiC = 2) and yield strength of the matrix (84.6 MPa

(12)

The theoretical strength is calculated to 178.41 MPa, which is a 17.8% error margin from the measured strength. The results of the theoretical estimation of the composite strength are summarized in Fig. 14a, and Table 2. The major contributors to the strength of the composites are determined to be dislocation strengthening (CTE mismatch and Orowan), load transfer, and grain refinement in that order. The difference between calculated and experimental values can be attributed to inaccuracies in selected

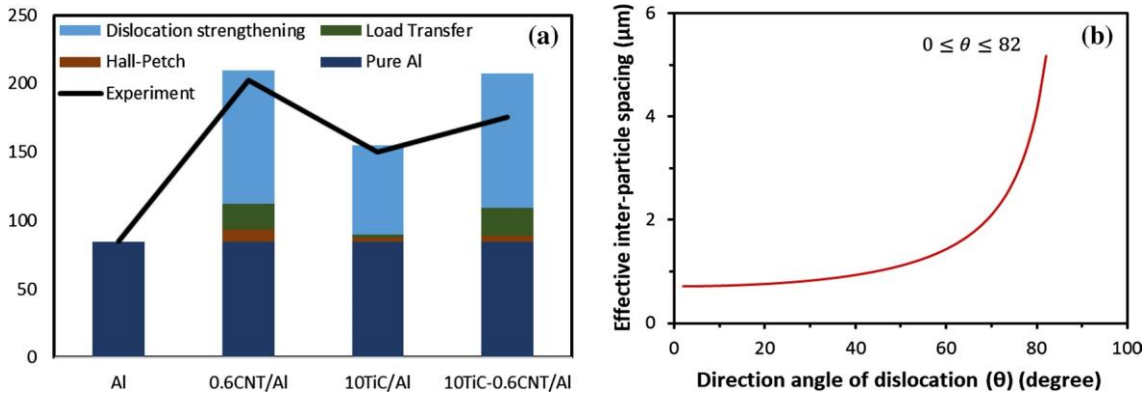

Fig. 14 Plot of **a** estimated strengthening mechanisms contribution to yield stress increase in composites, **b** the variation of effective inter-particle spacing with dislocation angle, θ between 0 and 82

Table 2 Summary of theoretical estimation of strengthening mechanism in studied composites

	Grain refinement (MPa)	Thermal mismatch (MPa)	Load transfer (MPa)	Orowan (MPa)	Total ($\sigma_m + \Delta\sigma_c$) (MPa)	Measured (MPa)	% Error
0.6CNT/Al	9.17	64.47	18.13	33.64	206.99	202.74	3.5
10TiC/Al	2.61	65.16	2.45	0.00	158.44	150.00	3.2
10TiC–0.6CNT/Al	4.32	97.65	20.57	33.65	178.41	175.75	17.8

parameters, and the presence of porosity in the experimental samples not accounted for in theoretical models. The presence of CNT agglomerations (Fig. 6e) also acts as crack initiation and propagation sites.

Another critical source of error arises from the Orowan-Ashby [53] model used to estimate the strengthening due to dislocation interaction with CNT reinforcement. The model is derived assuming spherical reinforcement shape with the parameter, as the effective planar inter-particle spacing. The inter-particle spacing controls how effec- tively a dislocation interacts with the reinforcement parti- cle and is dependent on the size (d_p) and volume fraction (V_f) of reinforcement. However, the cylindrical nature of CNTs makes the generalised effective inter-particle spacing approach based on spherical diameter inadequate for this type of reinforcement. The conversion of spherical model to cylindrical model using 2-dimensional system is well explained in details by Park et al. [48]. In extruded samples, the CNTs can be assumed to align with extrusion direction, while for sintered samples, it can be randomly distributed. The effective inter-particle spacing that inter- acts with an approaching dislocation varies according to the dislocation angle (θ), as presented in Fig. 14b. For complex microstructure such as a hybrid bimodal rein- forced composite, which combines particulate and short fiber reinforcement, generalized numerical models can introduce some significant errors.

The empirically derived numerical models used in theoretical estimation of strengthening mechanisms of composites maybe sensitive to length scales resolution, since it relies on macroscopic assumptions. For a bimodal hybrid reinforced composite consisting of microscopic-scale Al matrix, mesoscopic-scale TiC reinforcement, and microscopic-scale CNT reinforcement, the ability of the models to accurately evaluate the properties may be low. An effec- tive linkage between the different length scales is needed to understand the fundamental mechanisms and develop suitable numerical models. The effect of the different length scales on the effective properties of the composite can be better evaluated in multiscale analysis. This concept is carefully studied by Fadhil et al. [55] and in a book by Jinghong Fan [56]. The combination of simplifications in numerical models' formulation, such as that discussed above, porosity, reinforcement agglomeration, and effect of different length scales may have contributed to the high disparity between estimated and measured strength of hybrid composite.

3.4 Coefficient of Thermal Expansion (CTE)

In many materials, a change in temperature results in physical expansion or contraction. The CTE measures the change in a unit length of a bulk material resulting from a degree rise or fall in temperature. Figure 15 shows the variation of the CTE of pure Al, CNT/Al, TiC/Al, and TiC–CNT/Al composites

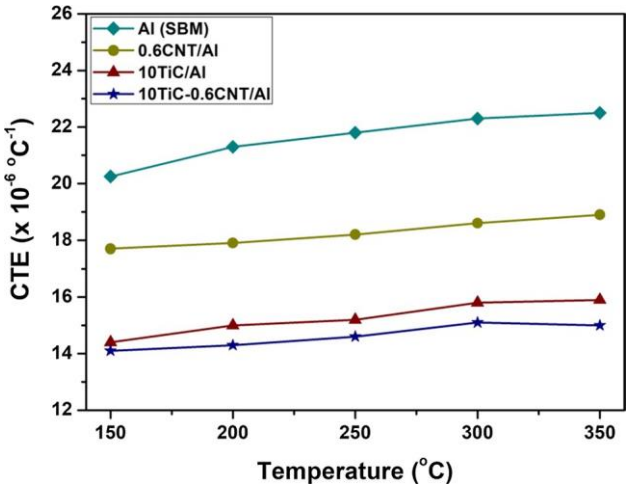

Fig. 15 CTE of pure Al, CNT/Al, TiC/Al and hybrid TiC–CNT/Al composites measured from 150 °C to 350 °C

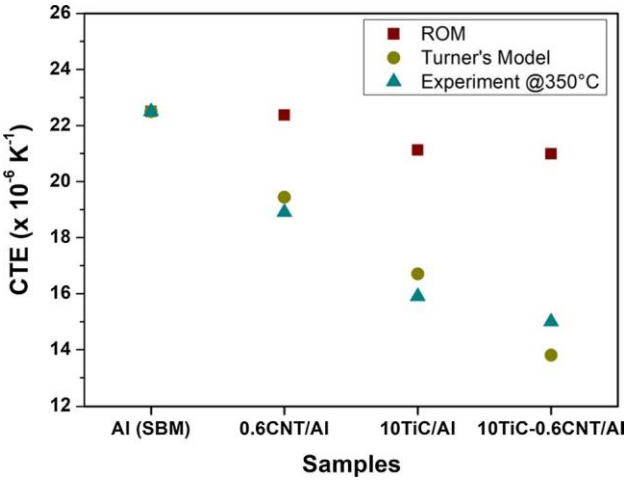

Fig. 16 Comparison between experimental measurement and theoretical calculation of CTE for CNT, TiC and hybrid reinforced Al matrix composites

when the temperature is increased from 150 to 350 °C. Generally, the CTE of all Al composites is superior to that of pure Al. It is clear from Fig. 15 that CNT/Al have higher CTE than TiC; this may be attributed to the weight percentage difference between them. The CTE of CNT/Al, TiC/Al, and hybrid TiC–CNT/Al composites decreased by approximately 16%, 29.3% and, 33.3%, respectively. It is clear from Fig. 15 that TiC–CNT/Al composite has the lowest CTE. This can be attributed to the intrinsically low CTE of ceramic, such as TiC and CNT (nearly zero) and their homogeneous distribution in the Al matrix. The presence of TiC and CNT hinders the growth of Al particles during heating, exerting effective pinning inside the matrix [57]. The linear decrease of CTE of pure Al with the addition of ceramic particles is explained by the theory that thermal expansion of Al matrix composites is governed by the competing interactions between the expansion of Al matrix and the constraint of reinforcement through their interfaces [58, 59].

Theoretical models such as the rule of mixture (ROM) (Eq. 13) and Turner's model (Eq. 14) for particles or continuous reinforcement [1, 38, 59] are frequently used to estimate the CTE of the CNT/Al, TiC/Al, and hybrid composites and compared with experimental results.

$$\varepsilon_c = \varepsilon_r V_r + \varepsilon_{Al}\ 100 - V_r \tag{13}$$

$$\varepsilon_c = \frac{E_r \varepsilon_r V_r + E_{Al} \varepsilon_{Al}\ 100 - V_r}{E\ V + E\quad 100 - V} \tag{14}$$

$$r\ \ r \qquad Al \qquad\quad r$$

where ε_c, ε_r (CNT 0 [25], TiC 7×10^{-6} K^{-1}) and ε_{Al} (22.5 [60]) are the CTE of Al composites, reinforcement, and Al respectively; E_r (800 GPa for CNT [61], 450 GPa for TiC and E_{Al} 69 GPa) are the elastic modulus of reinforcement and Al respectively; V_r is the reinforcement volume fraction. As shown in Fig. 16, there is no agreement between CTE values calculated by ROM and experimental values because ROM does not account for the complexity of reinforcement geometry and the interfacial thermal stress within the composite [38]. In sharp contrast, Turner's model calculated values are in good agreement with experimental results (Fig. 16), deviating slightly for hybrid reinforcement since the reinforcement properties were estimated using ROM. This model accounts for mechanical interaction between reinforcement and matrix phases but disregards the shape and distribution factor of reinforcement particles within the composite, which is true for low volume fractions addition as used in this work [1]. The good fit between theoretical and experimental results can be attributed to the uniform dispersion of reinforcement in the Al matrix.

4 Conclusions

Al matrix composites reinforced with bimodal-sized hybrid TiC–CNT were fabricated by solution ball milling and vacuum sintering. The measured wear resistance of TiC–CNT/Al composite was significantly higher than those reinforced with only CNT or TiC. The compressive yield strength of hybrid TiC–CNT/Al composite doubled compared to the Al matrix with no significant loss of ductility. Further, the

TiC–CNT/Al composite's CTE reduced by 33.3%, which is lower than that of CNT/Al and TiC/Al composites, thus providing excellent dimensional stability at elevated temperatures. Strengthening mechanisms contribution and CTE estimation models both showed good agreement with experimental values. The strength and ductility of materials are

usually mutually exclusive. Still, the use of bimodal hybrid reinforcement provides a promising strategy for the development of Al matrix composites with improved strength without significant loss of ductility. This will be useful in applications where good resistance to crack propagation is paramount.

Acknowledgements One of the authors (Peter Nyanor) would like to show appreciation to the Japan international cooperation agency (JICA) for the support towards his Ph.D. program at Egypt-Japan university of science and technology (EJUST) and powder technology division of central metallurgical research and development institute (CMRDI), Cairo-Egypt.

References

1. P.V. Trinh, N.V. Luan, D.D. Phuong, P.N. Minh, A. Weibel, D. Mesguich, C. Laurent, Compos. Part A-Appl. Sci. Manuf. **105**, 126 (2018)
2. M.O. Bodunrin, K.K. Alaneme, L.H. Chown, J. Mater. Res. Technol. **4**, 434 (2015)
3. O. Carvalho, M. Buciumeanu, S. Madeira, D. Soares, F.S. Silva, G. Miranda, Tribol. Int. **90**, 148 (2015)
4. O. Carvalho, M. Buciumeanu, S. Madeira, D. Soares, F.S. Silva, G. Miranda, Compos. Part B-Eng. **90**, 443 (2016)
5. A. Tan, J. Teng, X. Zeng, D. Fu, H. Zhang, Powder Metall. **60**, 66 (2017)
6. B. Vijaya Ramnath, C. Elanchezhian, M. Jaivignesh, S. Rajesh, C. Parswajinan, A. Siddique Ahmed Ghias, Mater. Des. **58**, 332 (2014)
7. O. El-Kady, H.M. Yehia, F. Nouh, Int. J. Refract. Met. Hard Mater. **79**, 108 (2019)
8. K.K. Alaneme, I.B. Akintunde, P.A. Olubambi, T.M. Adewale, J. Mater. Res. Technol. **2**, 60 (2013)
9. X. Chen, Z. Xu, D. Fu, H. Zhang, J. Teng, F. Jiang, Met. Mater. Int. (2020). https://doi.org/10.1007/s12540-019-00585-9
10. P. Nyanor, O. El-Kady, H.M. Yehia, A.S. Hamada, K. Nakamura, M.A. Hassan, Met. Mater. Int. (2019). https://doi.org/10.1007/s12540-019-00445-6
11. S.C. Tjong, Z.Y. Ma, Compos. Sci. Technol. **59**, 1117 (1999)
12. M.J. Shen, X.J. Wang, M.F. Zhang, X.S. Hu, M.Y. Zheng, K. Wu, Mater. Sci. Eng. A **601**, 58 (2014)
13. L.-J. Zhang, F. Qiu, J.-G. Wang, H.-Y. Wang, Q.-C. Jiang, Mater. Sci. Eng. A **637**, 70 (2015)
14. A. Chaubey, P. Konda Gokuldoss, Z. Wang, S. Scudino, N. Mukhopadhyay, J. Eckert, Technologies **4**, 37 (2016)
15. X. Zhang, S. Li, D. Pan, B. Pan, K. Kondoh, Compos. Part A-Appl. Sci. Manuf. **105**, 87 (2018)
16. W.J. Kim, Y.J. Yu, Scr. Mater. **72–73**, 25 (2014)
17. E.T. Thostenson, Z. Ren, T.-W. Chou, Compos. Sci. Technol. **61**, 1899 (2001)
18. A. Esawi, K. Morsi, Compos. Part A-Appl. Sci. Manuf. **38**, 646 (2007)
19. K. Ravi Kumar, K. Kiran, V.S. Sreebalaji, J. Alloys Compd. **723**, 795 (2017)
20. B. Chen, S. Li, H. Imai, L. Jia, J. Umeda, M. Takahashi, K. Kondoh, Mater. Des. **72**, 1 (2015)
21. H. Kwon, M. Estili, K. Takagi, T. Miyazaki, A. Kawasaki, Carbon **47**, 570 (2009)
22. H. Cui, X. Yan, M. Monasterio, F. Xing, J. Nanomater. **7**, 262 (2017)
23. J. Tang, G. Fan, Z. Li, X. Li, R. Xu, Y. Li, D. Zhang, W.-J. Moon, S.D. Kaloshkin, M. Churyukanova, Carbon **55**, 202 (2013)
24. X. Yao, J. Jiang, C. Xu, L. Zhou, C. Deng, J. Wang, Fibers Polym. **18**, 1323 (2017)
25. H. Kwon, D.H. Park, J.F. Silvain, A. Kawasaki, Compos. Sci. Technol. **70**, 546 (2010)
26. M.T.Z. Hassan, A.M.K. Esawi, S. Metwalli, J. Alloys Compd. **607**, 215 (2014)
27. H.M. Yehia, O.A. Elkady, Y. Reda, K.E. Ashraf, Trans. Indian Inst. Met. **72**, 85 (2019)
28. S.C. Tjong, Mater. Sci. Eng. R Rep. **74**, 281 (2013)
29. S.N. Alam, L. Kumar, Mater. Sci. Eng. A **667**, 16 (2016)
30. F. Saba, M. Haddad-Sabzevar, S.A. Sajjadi, F. Zhang, Powder Technol. **331**, 107 (2018)
31. Z. Baig, O. Mamat, M. Mustapha, Crit. Rev. Solid State **43**, 1 (2018)
32. Z.Y. Liu, S.J. Xu, B.L. Xiao, P. Xue, W.G. Wang, Z.Y. Ma, Compos. Part A-Appl. Sci. Manuf. **43**, 2161 (2012)
33. J. Fan, S. Xu, Iran. Polym. J. **27**, 339 (2018)
34. M. Chen, G. Fan, Z. Tan, D. Xiong, Q. Guo, Y. Su, J. Zhang, Z. Li, M. Naito, D. Zhang, Mater. Des. **142**, 288 (2018)
35. X. Chen, J. Tao, J. Yi, Y. Liu, C. Li, R. Bao, Mater. Sci. Eng. A **718**, 427 (2018)
36. N. Samer, J. Andrieux, B. Gardiola, N. Karnatak, O. Martin, H. Kurita, L. Chaffron, S. Gourdet, S. Lay, O. Dezellus, Compos. Part A-Appl. Sci. Manuf. **72**, 50 (2015)
37. X. Liu, C. Li, J. Eckert, K.G. Prashanth, O. Renk, L. Teng, Y. Liu, R. Bao, J. Tao, T. Shen, J. Yi, Mater. Charact. **133**, 122 (2017)
38. M. P. Reddy, M. A. Himyan, F. Ubaid, R. A. Shakoor, M. Vyasaraj, P. Gururaj, M. Yusuf, A. M. A. Mohamed, and M. Gupta, Ceram. Int. (2018)
39. X. Gao, H. Yue, E. Guo, S. Zhang, B. Wang, E. Guan, S. Song, H. Zhang, Mater. Sci. Tech.-Lond. **34**, 1 (2018)
40. Z.Y. Liu, B.L. Xiao, W.G. Wang, Z.Y. Ma, Compos. Part A-Appl. Sci. Manuf. **94**, 189 (2017)
41. O. El-Kady, A. Fathy, Mater. Des. **54**, 348 (2014)
42. J.-K. Wu, C.-C. Ye, T. Liu, Q.-F. An, Y.-H. Song, K.-R. Lee, W.-S. Hung, C.-J. Gao, Mater. Des. **119**, 38 (2017)
43. F. Ogawa, S. Yamamoto, C. Masuda, Mater. Sci. Eng. A **711**, 460 (2018)
44. M.K. Habibi, M. Paramsothy, A.M.S. Hamouda, M. Gupta, J. Mater. Sci. **46**, 4588 (2011)
45. A.D. Akinwekomi, W.-C. Law, C.-Y. Tang, L. Chen, C.-P. Tsui, Compos. Part B-Eng. **93**, 302 (2016)
46. J.F. Zhang, X.X. Zhang, Q.Z. Wang, B.L. Xiao, Z.Y. Ma, J. Mater. Sci. Technol. **34**, 627 (2018)
47. B. Chen, J. Shen, X. Ye, L. Jia, S. Li, J. Umeda, M. Takahashi, K. Kondoh, Acta Mater. **140**, 317 (2017)
48. J.G. Park, D.H. Keum, Y.H. Lee, Carbon **95**, 690 (2015)
49. M. Yang, L. Weng, H. Zhu, F. Zhang, T. Fan, D. Zhang, Sci. Rep. **7**, 1–10 (2017)
50. Y. Tang, X. Yang, R. Wang, M. Li, Mater. Sci. Eng. A **599**, 247 (2014)
51. A. Kelly, W. Tyson, J. Mech. Phys. Solids **13**, 329 (1965)
52. S. Xie, W. Li, Z. Pan, B. Chang, L. Sun, J. Phys. Chem. Solids **6**, 1153–1158 (2000)
53. M. Yang, L. Weng, H. Zhu, T. Fan, D. Zhang, Carbon **118**, 250 (2017)
54. X. Zhou, D. Su, C. Wu, L. Liu, J. Nanomater. **2012**, 1 (2012)
55. S.A. Fadhil, J.H. Azeez, M.A. Hassan, Indian J. Phys. (2020). https://doi.org/10.1007/s12648-020-01710-w
56. J. Fan, *Multiscale analysis of deformation and failure of materials: fan/multiscale analysis of deformation and failure of materials* (Wiley, Chichester, 2010)
57. X. Yang, T. Zou, C. Shi, E. Liu, C. He, N. Zhao, Mater. Sci. Eng. A **660**, 11 (2016)

58. P. Sharma, S. Sharma, D. Khanduja, J. Asian Ceram. Soc. **3**, 240 (2015)
59. P.R. Matli, F. Ubaid, R.A. Shakoor, G. Parande, V. Manakari, M. Yusuf, A.M. Amer Mohamed, M. Gupta, RSC Adv. **7**, 34401 (2017)
60. H. Ji, R. Mclendon, J.A. Hurtado, V. Oancea, J. Bi, Dassault Systèmes Simulia Corp.,U.S.A 26 (2018)
61. B.G. Demczyk, Y.M. Wang, J. Cumings, M. Hetman, W. Han, A. Zettl, R.O. Ritchie, Mater. Sci. Eng. A 6 (2002)